

A Plug and Play Solution Validated with Magnetic Resonance Velocimetry for Ensuring Optical Cleanliness in Powder Bed Fusion Systems

D. D. Borup¹, C. J. Elkins², J. Mireles³, H. H. Estrada^{3,4}, R. Wicker^{3,4}

¹ Borup Solutions LLC, Rochester, MN, USA

² Elkins Engineering LLC, Bozeman, MT, USA

³ W.M. Keck Center for 3D Innovation, University of Texas at El Paso, El Paso, TX, USA

⁴ Department of Aerospace & Mechanical Engineering, University of Texas at El Paso, El Paso, TX, USA

Abstract

It is widely known that in Laser Powder Bed Fusion (LPBF) systems, soot and other particulates become deposited on the optical window over time. This requires frequent and time-consuming cleanings to maintain system performance. In the present work, the flow field inside the Aconity MIDI+ LPBF system was studied using Magnetic Resonance Velocimetry (MRV). The results reveal that flow inside the system tends to circulate from the build plate into the optical cavity. To mitigate this, a proposed “shielding” component was designed to provide clean flow into the optical cavity. The design was implemented and measured using the MRV model. The addition of shielding supply pushed recirculating flow to the sides of the build chamber, rather than the optical cavity. This design thus has the potential to reduce the amount of deposition on the optical window, allowing for lower maintenance through less frequent cleanings.

Introduction

Laser powder bed fusion (LPBF) systems are an increasingly popular tool for additive manufacture of metal components in numerous industries, including oil & gas and aerospace. In LPBF systems, components are built by melting a thin layer of metal powder via application of a fiber laser at a power of hundreds of watts. Vapor and other byproducts produced during laser melting are known to negatively impact final build quality [1]. The two most commonly proposed mechanisms for this impact are attenuation of the laser by the vapor plume, which contains particles in the 10-150 nm diameter range, and redeposition of larger particles (spatter) on other areas of the build surface [2].

The most common technique to mitigate the impact of these byproducts is application of a directional inert gas flow across the build area. Recent work suggests that the speed and direction of gas flow can have a substantial impact on laser delivery [3], with multiple studies suggesting that faster, more uniform gas flow leads to improved final build quality [2, 4]. Reijonen et al. also conclude that the vapor plume, which is impacted by shielding gas flow, is sufficiently important that it must be included when modeling the melt pool geometry [5].

Particles in the 10-150 nm diameter range have a very slow settling velocity, on the order of millimeters per minute or slower, so it is likely that they will be carried far beyond the build surface once entrained in the flow. Depending on the secondary flows present in the build chamber, these particles may cross the laser path above the build surface or deposit on the protective window

between the build chamber and laser optics. While studies of such “long-range” contaminant transport are limited, it is common knowledge in the AM industry that the optics in LPBF systems require regular cleaning. A recent investigation into a detection system for monitoring protective window cleanliness [6] underscores the potential importance of this issue.

It is difficult to predict the secondary flows that will arise from a given inlet and outlet configuration in complex geometries such as those found inside of LPBF systems. Computational fluid dynamics (CFD) techniques are readily available for simulating such flows. However, CFD results depend heavily on proper setup and are difficult to validate. Hotwire anemometry has been used to carry out pointwise measurements [7], but single hot wires do not provide information regarding the flow direction and may be of limited value when trying to understand the structure of three-dimensional flows.

Magnetic Resonance Velocimetry (MRV) allows for measurement of the full, 3D velocity field in a matter of hours using a commercially available Magnetic Resonance Imaging (MRI) machine. While MRV uses water as the working fluid, dimensional analysis provides a reliable foundation for use of the technique to study gas flows. In the past two decades MRV has been used in numerous application areas across engineering and biomechanics—for example, as summarized by Gladden and Sederman [8]. More recently, the repeatability of MRV between locations and MRI systems was demonstrated in a pair of multi-site studies [9].

In a 2023 study, MRV was applied to examine the full, 3D velocity field for shielding gas flow in an EOS M290 system. The resulting insights were used to re-design the gas inlet to produce more uniform flow over the build surface, which led to improved part quality across the build surface [10]. The MRV results in the study also captured secondary and recirculating flow structures arising due to the inlet and outlet geometries in the build chamber. The present study followed a very similar design procedure: the MIDI+ system was reverse engineered to create a flow model, which was then printed using vat photopolymerization and used for MRV measurements to assess the flow field.

Methods and Materials

Aconity MIDI+ Laser Powder Bed Fusion System

The Aconity MIDI+ system (Aconity 3D GmbH) is the subject of this study. The MIDI+ has a build volume 250 mm in diameter by 250 mm in height and uses either argon or nitrogen inert gas at a positive chamber pressure of 6000 mbar, with a typical residual oxygen content below 100 ppm.

Aconity MIDI+ Flow Models

A CAD model of the MIDI+ system was scaled down by a ratio of 1:4 to produce the flow models used in this study. Scaling was needed so that the models would fit inside the MRI coil, which is around 280 mm in diameter. Models were printed via vat photopolymerization in a Stratasys Neo 450 3D printer (Stratasys, Eden Prairie, MN, USA) using DSM Somos Watershed 11122 polymer (DSM, Heerlen, Netherlands). The use of plastic construction required increasing

the thickness of most walls relative to the original (scaled) size. The minimum thickness for successful fabrication (1 mm) was used as a general guideline for internal structures and holes, while the external walls were designed with thicknesses of 7 mm or greater to ensure sufficient strength against internal pressure. All thickening was carried out while preserving the internal geometries of the system, including all flow passageways, wall cavities, and the recoater.

Two models were printed: the baseline model, which had no modifications other than those described above; and the modified model, which contained an additional “shielding manifold” that provided two inlet vents in the region of the optical (laser) window. Figure 1 shows multiple views of both models, with important features labeled.

The shielding manifold (shown in orange in Fig. 1b) was designed to supply uncontaminated flow to the optical cavity via two independently fed and metered inlets. The use of two inlets was chosen to provide stronger protection than a single vent could provide; the primary (upper) inlet was aimed directly onto the laser window, while the secondary (lower) inlet protected against entrainment of contaminated gas into the primary stream. An additional benefit of multiple independent inlets was greater operating flexibility for future optimization of the flow rates.

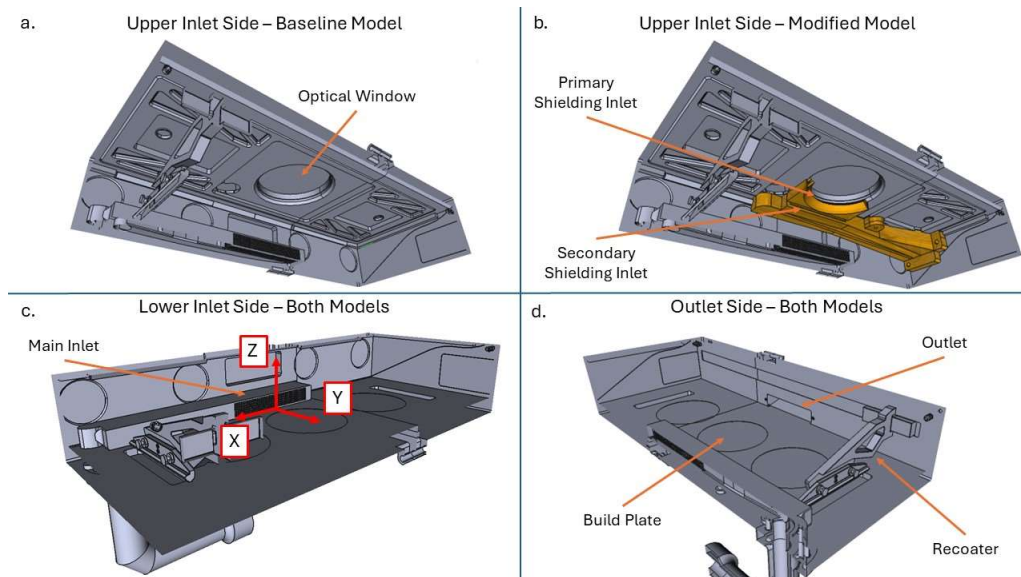


Figure 1: Cut-away views of MIDI+ flow models. (a) Top front portion of baseline model showing optical window with no shielding vent present, and (b) of modified model with added vent piece (orange) to supply primary and secondary shielding flows; (c) bottom front portion showing main inlet and coordinate system with origin at center of inlet along bottom wall; (d) bottom back portion showing recoater, build plate, and outlet.

Flow Loop Setup

The baseline flow model was connected to a standard MRV flow loop. On the inlet side, the flow loop consisted of: an 11 gallon reservoir tank; a 1/2 hp centrifugal pump (Little Giant TE-6-MD-SC series; Franklin Electric, Fort Wayne, IN, USA); a gate valve for flow metering; a 0.25 m section of 12.7 mm *outer* diameter, unbraided PVC tubing (Tygon E-6306) for flow monitoring; and 5 m of 12.7 mm internal diameter braided PVC tubing. The outlet side consisted only of an

additional 5 m of 12.7 mm ID tubing connected to the reservoir. Flow was monitored using a clamp-on ultrasonic flow meter (Model ME-8PXL; Transonic Systems Inc, Ithaca, NY, USA).

The main flow inlet and outlet for the modified model were connected to the same flow loop. The primary and secondary shielding inlets were supplied by two 1/8 hp centrifugal pump (Little Giant 5-MD series). The lines were monitored using ME-6PXL (primary) and ME-5PXL (secondary) flow probes on short sections of E-6303 tubing of the appropriate diameter and metered using gate valves.

Temperature control of the working fluid was achieved by monitoring the reservoir temperature with a handheld thermometer. Bagged ice was placed into the reservoir as needed to maintain a temperature between 21 and 23 degrees Celsius.

Flow Measurements

Flow measurements were made using MRV, as described in detail in Elkins & Alley [11], to provide the 3-component mean velocity field over the entire volume. All data were collected on a 3 Tesla GE Signa MRI system (GE Healthcare, Waukesha, WI, USA) located at the Richard M. Lucas Center for Imaging at Stanford University.

Data were collected in two separate scan sessions: one for the baseline model, and a second for the modified model. Data were acquired on a Cartesian grid with 1 mm isotropic resolution on a 340 mm × 198 mm × 106 mm matrix. Manual rotation and translation of the datasets were performed to align the baseline and modified models for comparison purposes. Each scan session required approximately 42 minutes of data collection.

The coordinate system used to present data is shown in Fig. 1c. The origin is located at the spanwise (x -direction) center of the main inlet along the bottom wall of the model. The terms u , v , and w are used to refer to the x , y , and z velocity components, respectively, while the bold symbol \mathbf{u} refers to the 3-component velocity vector.

The target flow had a Reynolds number of 7000 based on the bulk flow through the inlet tube, which has a diameter of 50 mm in the full-size MIDI+ system (12.5 mm in the quarter-scale model). Matching the Reynolds number ensures that the flow field and normalized velocity values obtained using MRV are identical to the those in the full-scale system, according to the principle of dimensional analysis. To achieve this Reynolds number in the MRV model, flow was supplied to the main inlet at 4.1 liters per minute. This produced an average velocity of $U_{bulk} = 8.2$ cm/s at the inlet. The same main inlet flow rate was used for all experiments.

In the modified model, the flow rate supplied to each shielding inlet was 0.8 liters per minute. This value was chosen to achieve an average velocity matching U_{bulk} given above. Two flow configurations were tested: a “dual-flow” configuration with both primary and secondary shielding inlets supplied and a “single-flow” configuration with flow supplied only to the primary shielding inlet. All velocity data are presented after normalizing by the bulk velocity, U_{bulk} , to produce dimensionless velocity values; normalization is denoted with a tilde (e.g., \tilde{u}).

Results and Discussion

Baseline Flow Field

Figure 2 shows a three-dimensional iso-contour at $|\vec{u}| = 0.5$ for flow inside the baseline model. Flow enters at the bottom left and proceeds across the build surface. The boundary layer height is relatively constant across the width of the build plate (x direction) although it grows thicker as it proceeds across the plate in the y direction. After traversing the build plate, a large secondary flow structure causes some of the flow to spread outward and upward along the back wall, away from the exit plenum. Small particles or other contaminants entrained above the build plate could be spread around the build chamber in this manner, quickly reaching the optical cavity via the upward secondary flow.

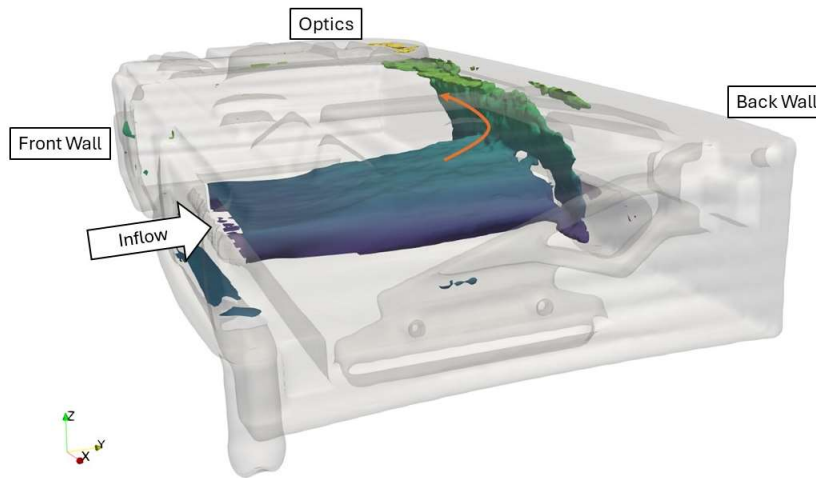


Figure 2: Iso-contour of normalized velocity magnitude, $|\vec{u}| = 0.5$, in the baseline model. The main flow over the build plate (with variable boundary layer) and secondary flow up the back wall of the build chamber are visible. Orange arrow indicates the general direction of the flow inside the isocontour.

Figure 3 shows the flow field in the centerplane of the build chamber in more detail. The streamwise velocity component, \vec{v} , is shown on a diverging red/blue color scale to highlight areas of reversed flow ($v <_e 0$). The large blue area in the top half of the slice indicates the presence of a large region of such flow extending all the way back to the inlet side of the of the build chamber. In other words, a recirculation cell was present along the centerplane that spanned the entire height and width of the chamber.

Another view of the flow can be seen in Figure 4, which shows the same values (streamwise velocity, \vec{v}) in a horizontal plane at $z = 7.5$ mm above the build plate. This plane lies at the mid-height of the main inlet and corresponds to 30 mm above the build plate in the full-scale model. Several features of the flow field are evident. The fast core of gas is evident between the inlet and outlet, passing over almost the entire width of build plate. Flow on either side of the core is slower, with a central region of forward flow and peripheral regions of slow reversed flow along each side.

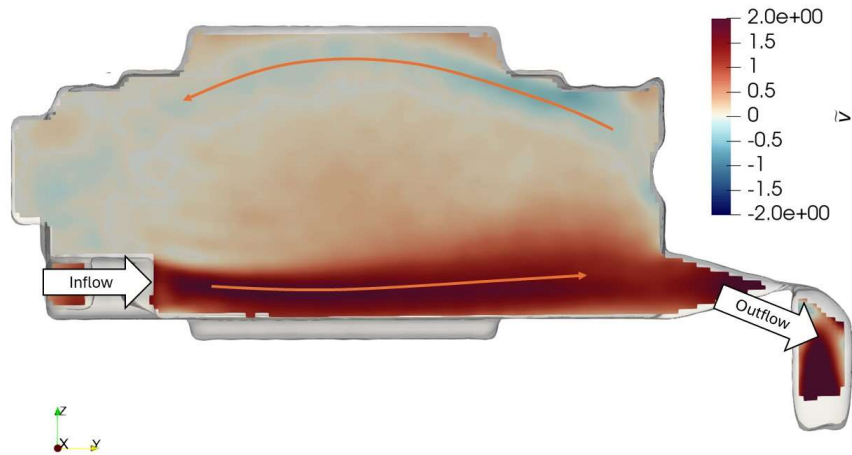


Figure 3: Centerplane view of baseline model flow with color contours showing streamwise velocity component, \bar{v}_x , on a diverging scale. Blue regions represent reversed flow. Orange arrows indicate the general direction of the flow in key regions.

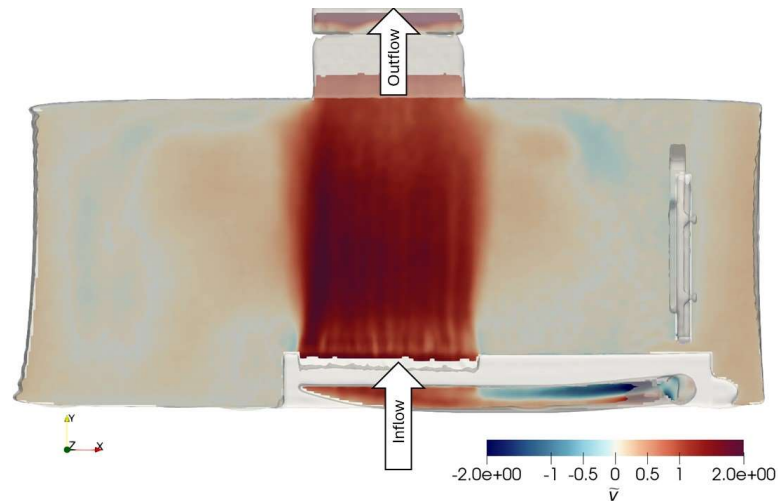


Figure 4: Color contours of streamwise velocity, \bar{v}_x , at mid-height of main inlet, 7.5 mm above build plane (30 mm in full-scale MIDI+ system). Blue regions represent reversed flow.

Overall, while the results show good flow speed and uniformity across the build plate, they also reveal that the MIDI+ flow design produces a large recirculating flow structure oriented in the vertical direction. Such a structure provides a short path for contaminants entrained above the build plate to be carried into the optical cavity. This could lead to undesirable laser attenuation by particles suspended in the gas, as well as those deposited on the optical window.

Effect of Shielding Inlets

Figures 5 and 6 are identical to Fig. 2 for the single- and dual-flow configurations, respectively. These 3D iso-surfaces provide a rough overview of the fastest flow regions in three

dimensions. In the single-flow case (Fig. 5), the shielding flow is fairly fast inside the optical cavity but loses momentum elsewhere. The recirculation structure generated by the main flow is similar in shape, but interaction with the shielding flow causes it to remain constrained near the back wall rather than extending along the top wall of the chamber.

In the dual-flow case (Fig. 6), the shielding flow is strong enough to retain momentum through the optical cavity and approach the outlet as a coherent jet. The recirculation structure produced by the main flow is altered considerably, with secondary flow forced laterally along the back wall towards the recoater, rather than upwards towards the optical cavity. The shielding flows thus appear to provide two benefits in this case: first, the optical cavity experiences a consistent supply of clean flow from the vents themselves; second, recirculating contaminated air is redirected away from the optical cavity and laser path.

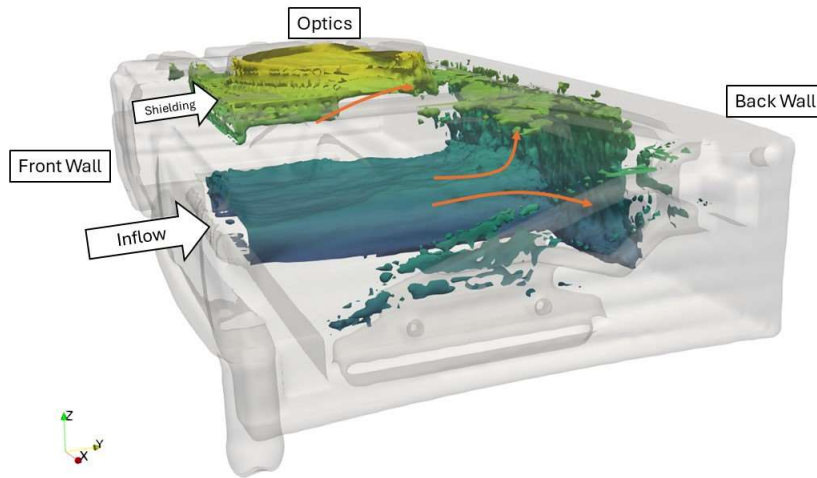


Figure 5: Iso-contour of normalized velocity magnitude, $|\tilde{u}| = 0.5$, in the modified model with single-flow configuration. The main flow over the build plate (with variable boundary layer), shielding flow into the optical cavity, and secondary flow up the back wall of the build chamber are visible. Orange arrows indicate the general direction of the flow in key regions.

Views of the centerplane, with diverging color contours of \tilde{v} (similar to Fig. 3) are shown in Figs. 7 and 8. Changes in the secondary flow structure due to the shielding vent(s) are again evident. In the single-flow configuration (Fig. 7), reversed flow is still present but confined to two regions: the upper corner downstream of the optical cavity (top right, in the figure), and the center of the build chamber. The latter region is still undesirable as any contaminants carried into this region could still cross the laser path. In the dual-flow configuration (Fig. 8), however, there is very little reversed flow in the centerplane. This suggests once again that flow along the back wall is being pushed laterally into one or both sides of the build chamber in the dual-flow configuration.

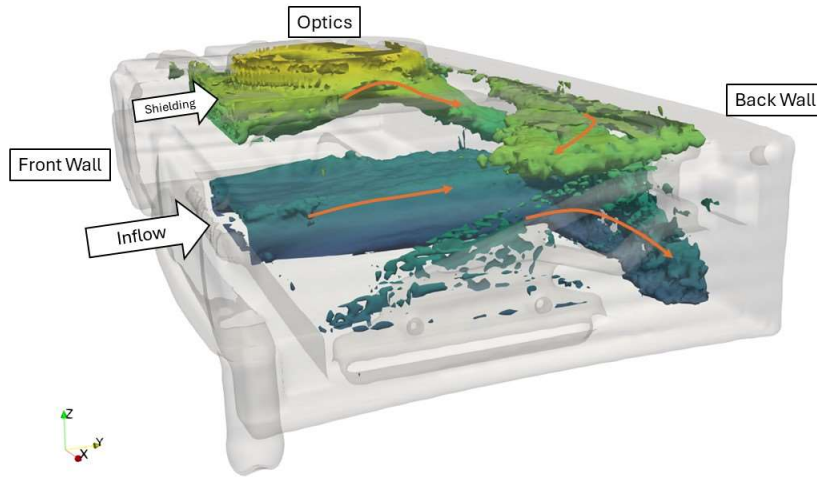


Figure 6: Iso-contour of normalized velocity magnitude, $|\tilde{\mathbf{u}}| = 0.5$, in the modified model with dual-flow configuration. The main flow over the build plate (with variable boundary layer) and shielding flows through the optical cavity are visible, while the secondary flow is observed to be pushed laterally towards the near wall and recoater. Orange arrows indicate the general direction of the flow in key regions.

A quantitative comparison of all cases is found in Fig. 9. Streamwise velocity, \tilde{v} (horizontal axis), is shown versus vertical position above the center of the build plate, z (vertical axis). Minimal differences were present in the core flow immediately above the build plate ($0 \leq z \leq 10$). The maximum velocity was identical to baseline in the single-flow case and only 5% lower in the dual-flow case, while the location of the velocity peak was shifted around 1 mm closer to the build plate in both shielded cases. The differences in the upper portion of the build chamber are more pronounced. In the baseline case, forward flow was present up to $z = 50$, with a region of reversed flow inside the optical cavity ($z > 50$). In the modified design, a relatively quiescent area was present from $z = 20$ to 40, with strong *forward* flow present inside the optical cavity.

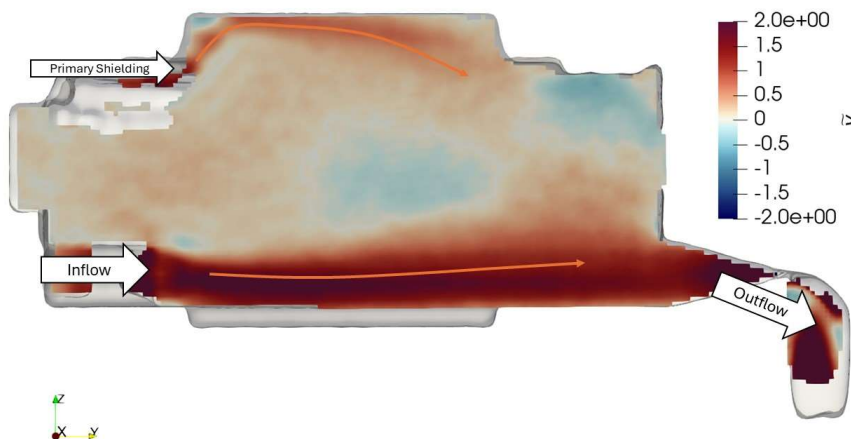


Figure 7: Centerplane view of modified model in single-flow configuration. Color contours show the streamwise velocity component, \tilde{v} , on a diverging scale. Orange arrows indicate the general direction of the flow in key regions.

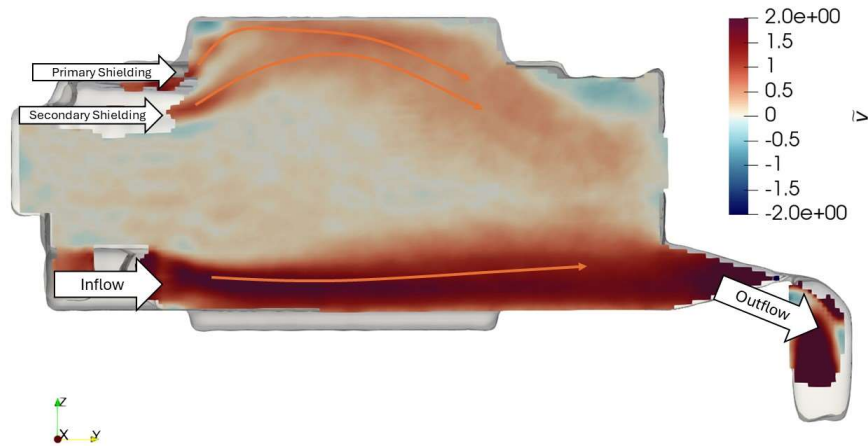


Figure 8: Centerplane view of modified model in dual-flow configuration. Color contours show the streamwise velocity component, \tilde{v} , on a diverging scale. Orange arrows indicate the general direction of the flow in key regions.

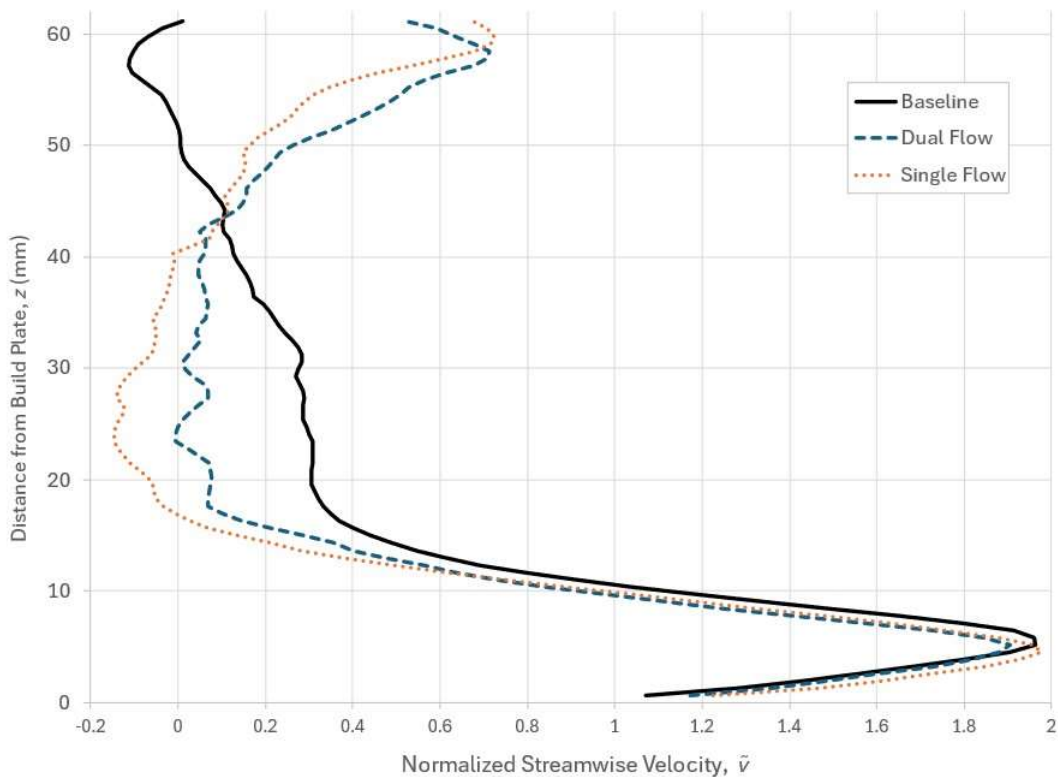


Figure 9: Comparison of normalized streamwise velocity, \tilde{v} , on a vertical line extending upward from the center of the build plate.

Figures 10 and 11 show additional changes to the flow versus the baseline case in the area of the build plate, as in Fig. 4. In both cases, the shape of the core flow over the plate was relatively un-changed when compared to the baseline. This is an important result as it suggests little impact of the shielding manifold on the main function of the directional gas flow. More pronounced

differences were observed in the secondary flow regions. In the single-flow case, the flow was somewhat asymmetric, with reversed flow primarily found on the recoater side of the build chamber. In the dual-flow case, strong reversed flow was present immediately on both sides of the build plate, extending all the way to both sidewalls.

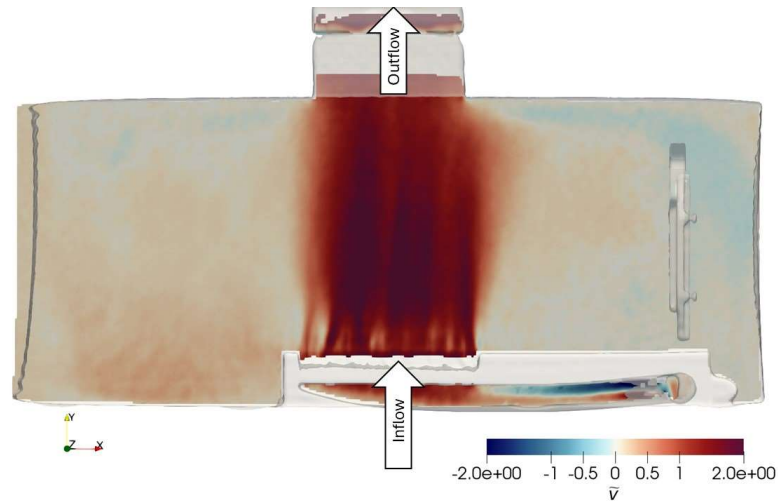


Figure 10: Color contours of streamwise velocity, \bar{v} , at mid-height of main inlet, 7.5 mm above build plane (30 mm in full-scale MIDI+ system), for the single-flow shielding configuration. Blue regions represent reversed flow.

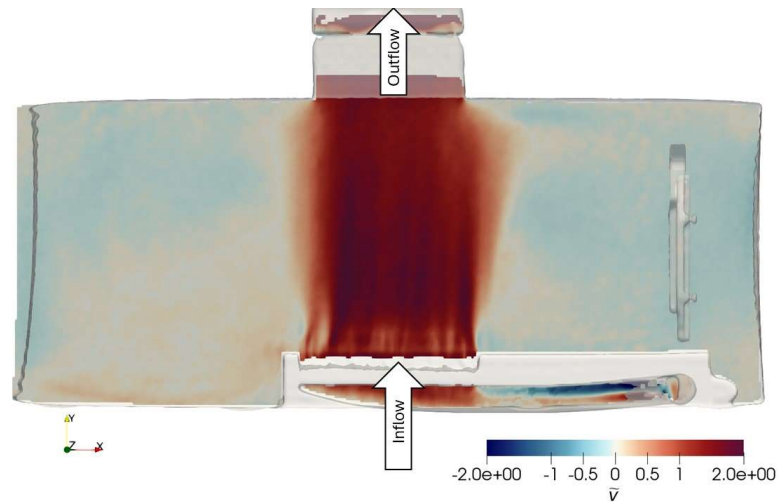


Figure 11: Color contours of streamwise velocity, \bar{v} , at mid-height of main inlet, 7.5 mm above build plane (30 mm in full-scale MIDI+ system), for the dual-flow shielding configuration. Blue regions represent reversed flow.

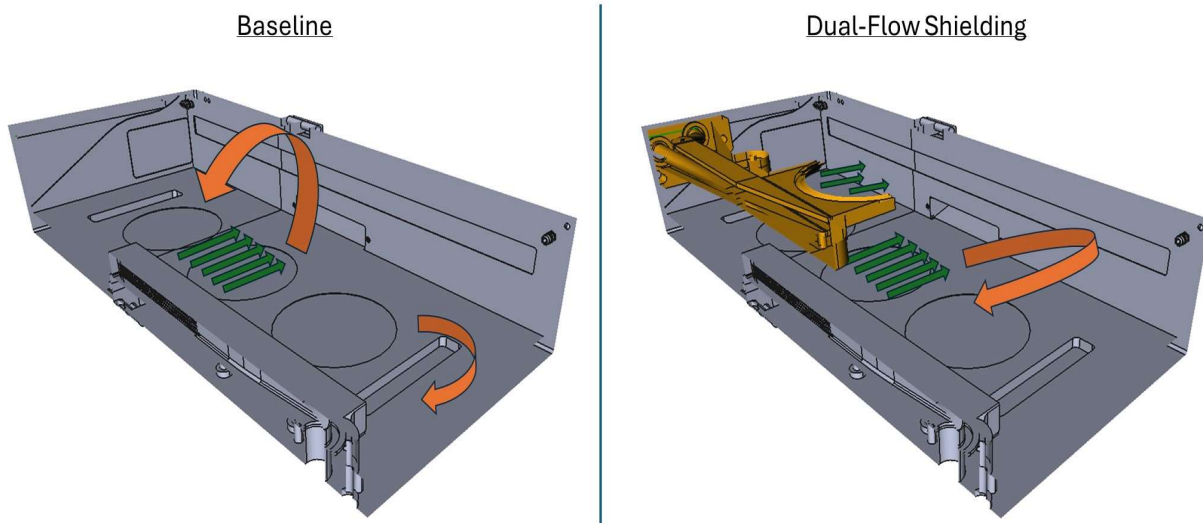


Figure 12: Simplified schematic of secondary flow patterns in baseline and dual-flow shielding cases. Green arrows represent flow of clean gas, while orange arrows represent recirculation regions that may contain contaminants entrained above or to the side of the build plate.

Finally, simplified representations of the flow pattern observed with and without the shielding manifold are provided in Fig. 12. In the baseline case, the main flow across the build plate produces a recirculation cell with a horizontal axis of rotation that carries reversed flow through the optical cavity and directly across the laser path. With dual-flow shielding, this cell was not present. Instead, a pair of recirculation cells were observed on either side of the build chamber. This would act to carry any contaminated recirculating flow towards the sides of the build chamber. The single-flow case (not shown in Fig. 12) exhibited a mix of both behaviors, with a smaller vortex contained above the outlet and a spanwise cell along the recoater side of the build chamber. The pronounced differences observed between the single and dual-flow cases suggest that the flow rates to each shielding inlet could be optimized to minimize overall secondary flows.

Conclusions

Cleaning the optics of PBF-LB/M systems is a generally accepted practice to remove any contaminants that may accumulate on the laser window. The pattern of shielding gas flow is a likely contributor to such accumulation as recirculating gas may act to carry contaminants away from the build area and into other parts of the build chamber. The present study demonstrates that full-field MRV data can be used to characterize the baseline flow of shielding gas in any PBF-LB/M system as well as to design and validate flow modifications aimed at reducing laser attenuation due to contaminants.

Three-dimensional flow data obtained using MRV within a scale model of the Aconity MIDI+ system show that significant recirculation occurs inside the build chamber and could act to carry contaminants from the build area into the optical cavity. This is a likely mechanism for laser attenuation as the laser path is blocked by both the contaminated gas itself and deposition of contaminants on the protective window.

Introduction of one or two additional flow streams into the optical cavity via an add-on “shielding” manifold produced beneficial changes in the flow patterns inside the build chamber. The introduction of fluid into the optical cavity prevented reversed flow in this region, even when only one of the two shielding inlets was active. With both inlets active, the recirculation cell present in the baseline model was no longer observed; it was replaced by a pair of strong recirculation cells into the two sides of the build chamber. While these cells could still act to carry contaminants around the build chamber, they do not provide a direct path to reach the optical region.

Importantly, minimal changes were observed in the flow field immediately above the build plate after introduction of one or both shielding flows. This suggests that the addition of a shielding manifold would not compromise the primary function of the directional gas flow over the build plate, which is to remove contaminants quickly as they are generated by laser melting of the powder bed.

The “plug-and-play” solution presented here required an increase in flow rate of at most 40%, with no modifications to the internal build chamber other than attachment points to support and supply flow to the new manifold. Future work is needed to implement and test the proposed design on an actual MIDI+ system, and to determine the minimum shielding gas flow rates required to protect the optical cavity. If successfully validated at full-scale, the present design could be implemented quickly and easily on any existing MIDI+ system, leading to improved build quality and reduced cleaning frequency. In addition, the design approach and general principle of a “shielding flow” directed at the optical region could be generalized to other PBF-LB/M systems, as long as care is taken to account for each system’s baseline flow field.

Acknowledgements

The authors are grateful to the Richard M. Lucas Center for Imaging for use of MRI scanner time. This material is based on research sponsored by Air Force Research Laboratory under agreement number FA8650-20-2-5700. The U.S. Government is authorized to reproduce and distribute reprints for Governmental purposes notwithstanding any copyright notation thereon. The views and conclusions contained herein are those of the authors and should not be interpreted as necessarily representing the official policies or endorsements, either expressed or implied, of Air Force Research Laboratory or the U.S. Government.

References

- [1] B. Ferrar, L. Mullen, E. Jones, R. Stamp, C. Sutcliffe, Gas flow effects on selective laser melting (slm) manufacturing performance, *Journal of Materials Processing Technology* 212 (2012) 355–364.
- [2] A. Ladewig, G. Schlick, M. Fisser, V. Schulze, U. Glatzel, Influence of the shielding gas flow on the removal of process by-products in the selective laser melting process, *Additive Manufacturing* 10 (2016) 1–9.
- [3] D. Deisenroth, J. Neira, J. Weaver, H. Yeung, Effects of shield gas flow on meltpool variability and signature in scanned laser melting, in: *Proceedings of the ASME 2020 15th International Manufacturing Science and Engineering Conference*, p. V001T01A017.

- [4] H. Shen, P. Rometsch, X. Wu, A. Huang, Influence of gas flow speed on laser plume attenuation and powder bed particle pickup in laser powder bed fusion, *Jom* 72 (2020) 1039–1051.
- [5] J. Reijonen, A. Revuelta, T. Riipinen, K. Ruusuvoori, P. Puukko, On the effect of shielding gas flow on porosity and melt pool geometry in laser powder bed fusion additive manufacturing, *Additive Manufacturing* 32 (2020) 101030.
- [6] N. Praetzs, H. Sturzebecher, N. Pirch, F. Fischer, C. L. Haefner, Detection of contamination of protective windows in Laser Powder Bed Fusion by means of a line scan camera, in: C. W. Carr, V. E. Gruzdev, D. Ristau, C. S. Menoni (Eds.), *Laser-Induced Damage in Optical Materials 2021*, volume 11910, International Society for Optics and Photonics, SPIE, 2021, p. 1191015.
- [7] M. Schniedenham, F. Wiedemann, J. H. Schleifenbaum, Visualization of the shielding gas flow in slm machines by space-resolved thermal anemometry, *Rapid Prototyping Journal* 24 (2018) 1296–1304.
- [8] L. F. Gladden, A. J. Sederman, Recent advances in flow mri, *Journal of Magnetic Resonance* 229 (2013) 2–11.
- [9] M. J. Benson, A. J. Banko, C. J. Elkins, D.-G. An, S. Song, M. Bruscheckski, S. Grundmann, T. Bandopadhyay, L. V. Roca, B. Sutton, et al., Mrv challenge 2: phase locked turbulent measurements in a roughness array, *Experiments in Fluids* 64 (2023) 28.
- [10] C. Elkins, J. Mireles, H. Estrada, D. Morgan, H. Taylor, R. Wicker, Resolving the three-dimensional flow field within commercial metal additive manufacturing machines: Application of experimental magnetic resonance velocimetry, *Additive Manufacturing* 73 (2023) 103651.
- [11] Elkins, C. J., and Alley, M. T., Magnetic Resonance Velocimetry: Applications of Magnetic Resonance Imaging in the Measurement of Fluid Motion. *Experiments in Fluids*, Vol. 43, No. 6, 2007, pp. 823–858. <https://doi.org/10.1007/s00348-007-0383-2>